CHAPTER 6

MULTISCALE MODELING OF CONTACT-INDUCED PLASTICITY IN NANOCRYSTALLINE METALS

VIRGINIE DUPONT[1] AND FREDERIC SANSOZ[2]

[1]*School of Engineering, University of Vermont, Burlington, VT 05405, USA, e-mail: virginiedupont@gmail.com*

[2]*School of Engineering and Materials Science Program, University of Vermont, Burlington, VT 05405, USA,e-mail: frederic.sansoz@uvm.edu*

Abstract: Predicting the integrity of metallic thin films deposited on semiconductors for micro-electromechanical systems (MEMS) applications requires a precise understanding of surface effects on plasticity in materials with nano-sized grains. Experimentally, the use of nanoscale contact probes has been very successful to characterize the dependence of flow stress on mean grain size in nanocrystalline metals. From atomistic simulations, several models of plastic yielding for metal indentation have also been proposed based on the nucleation and propagation of lattice dislocations, and their interaction with grain boundaries beneath penetrating tips. However, model refinement is needed to include the characteristics of materials whose grain size is much smaller than the typical plastic zones found in contact experiments. Particularly, cooperative deformation processes mediated by grain boundaries, such as grain rotation, deformation twinning, and stress-driven grain coarsening, can simultaneously emerge for very small grain sizes (< 20 nm), thus making a predictive understanding of plastic yielding elusive. This chapter summarizes our recent progress in using multiscale modeling to gain fundamental insight into the underlying mechanisms of surface plasticity in nanocrystalline face-centered cubic metals deformed by nanoscale contact probes. Two numerical approaches to model contact-induced plasticity in nanocrystalline materials, the quasicontinuum method and parallel molecular dynamics simulation, are reviewed. Using these techniques, we discuss the role of a grain boundary network on the incipient plasticity of nanocrystalline Al films deformed by wedge-like cylindrical tips, as well as the processes of stress-driven grain growth in nanocrystalline films subjected to nanoindentation

Keywords: Nanoindentation, Nanocrystalline metal, Atomistic simulation

6.1. INTRODUCTION

Nanocrystalline films of pure face-centered cubic (FCC) metals such as Al, Ni and Cu with a grain size less than 100 nm, are commonly used in surface-micromachining to process micron-scale structures and devices including micro-electromechanical systems (MEMS) [1–5]. Characterizing the mechanical and

T. Dumitrica (ed.), Trends in Computational Nanomechanics, 151–172.
DOI 10.1007/978-1-4020-9785-0_6,

tribological behavior of nanocrystalline metals upon contact loading remains an essential task in predicting the structural integrity of such micro-components [6, 7]. In addition, past studies [8–10] have proved that a marked transition in plasticity mechanisms operates with a reduction of grain size from the microcrystalline to the nanocrystalline regime in FCC metals.

While advanced characterization techniques have been used to study the mechanical behavior of thin films, such as MEMS-based tensile testing [11–14] or membrane deflection experiments [15], small-scale contact experiments, such as nanoindentation, have been used ubiquitously to characterize the nature of yield phenomena and the influence of grain size on hardness and strengthening in nanocrystalline metals [16–22]. A nanoscale tip attached to the cantilever beam of an atomic force microscope (AFM) that was made to measure the nanomechanical behavior of metallic thin films is shown in Figure 6-1 along with nanoscale indentations performed on a nanocrystalline Ni surface. Such probes are particularly well-suited for the studies of plasticity transition in nanograined metals, because they can be highly sensitive to the heterogeneous nature of plastic deformation in very confined volumes of materials.

In earlier studies [9, 24, 25], particular focus has been placed on examining how dislocations interact with surrounding grain boundaries (GBs) by performing nano-indentations at the center of single nanograins, that is, by forcing the contact area to be much smaller than the grain size. Yang and Vehoff [25] have observed that the dislocations, which nucleate below the tip, only interact directly with the neighboring interfaces for grain sizes below 900 nm. At this scale, the point of elastic instability is clearly defined by a pop-in event whose width is strongly correlated to the size of the indented grain. The smaller the grain size, the smaller the pop-in width and the harder the material. For grain sizes comparable to the contact area, Minor et al. [24] have also revealed using in situ transmission electron microscopy (TEM) nanoindentation that significant dislocation activity could take

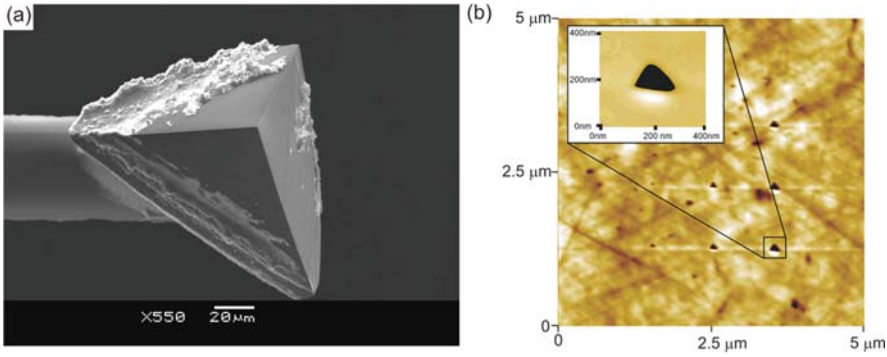

Figure 6-1. Measurements of nanomechanical properties in thin films using nanoscale contact probes. (**a**) SEM image of a made-to-measure cube-corner tip attached to the cantilever beam of an AFM; (**b**) AFM-enabled nanoscale indentations performed on a 50-μm-thick nanocrystalline Ni film [23]

place in ultrafine-grained Al thin films before the first obvious jump in displacement in the load-depth nanoindentation curves. However, a predictive understanding of plastic yielding in nanocrystalline metals during indentation remains elusive, primarily for two reasons:

- While the nanoscale indentations shown in Figure 6-1b can be considered as physically small, these contact zones can still be an order of magnitude larger than the mean grain size of the film tested. In this case, it is the cooperative deformation of the dense GB network that dominates the plastic behavior in nanocrystalline materials. All experimental evidence shows that the pile-up of deformation left around residual impressions varies dramatically from homogeneous at large grain size (> 20 nm) to inhomogeneous with intense plastic deformation in highly-localized shear bands for very small grain sizes (< 20 nm) [9, 21, 26, 27]. Furthermore, new deformation mechanisms, including grain rotation, deformation twinning, and stress-driven grain coarsening, can simultaneously emerge for very small grain sizes [28–32]. Therefore, some model refinement is required in order to include the characteristics of materials whose grain size is much smaller than the typical plastic zones found in contact experiments.
- GB-mediated deformation phenomena have been observed during the nanoindentation of nanocrystalline FCC metals. Abnormal grain growth was found by Jin et al. [29] during in situ TEM experiments of nanoindentation in nanocrystalline Al films. For instance, Figure 6-2 shows different snapshots from Jin et al.'s study, where a local increase in brightness related to grain rotation, indicates that grain growth takes place under the tip as indentation proceeds. Stress-driven grain growth was also observed by Zhang et al. [30, 31] during the micro-indentation of nanocrystalline Cu films. These authors showed that grain growth occurred at faster rates at cryogenic temperature than at room temperature, and that the purity of the material influences the grain growth process. Since it is well-established that the flow stress characterized by hardness testing strongly depends on the material grain size [8, 33–35], the process of contact-induced grain growth appears to be undesirable for most microscale systems with nanocrystalline characteristics. It is therefore critically important to understand the mechanisms of GB motion under nanoscale contact in order to achieve control over such phenomena.

This chapter presents an overview of quasicontinuum (QC) method and large-scale molecular dynamics (MD) simulations used to shed light on the fundamental mechanisms of surface plasticity in pure nanocrystalline metals deformed by nanoscale tips. The numerical methods related to the atomistic modeling of nanoscale contact in nanocrystalline films are reviewed in Section 6.2. Section 6.3 describes the effects of interatomic potentials on randomly-oriented microstructures and the energies at GBs predicted by atomistic simulation. Using the QC method, we focus in Section 6.4 on the role of a GB network on the incipient plasticity of a 7 nm-grain-size nanocrystalline Al film deformed by a wedge-like cylindrical tip. In

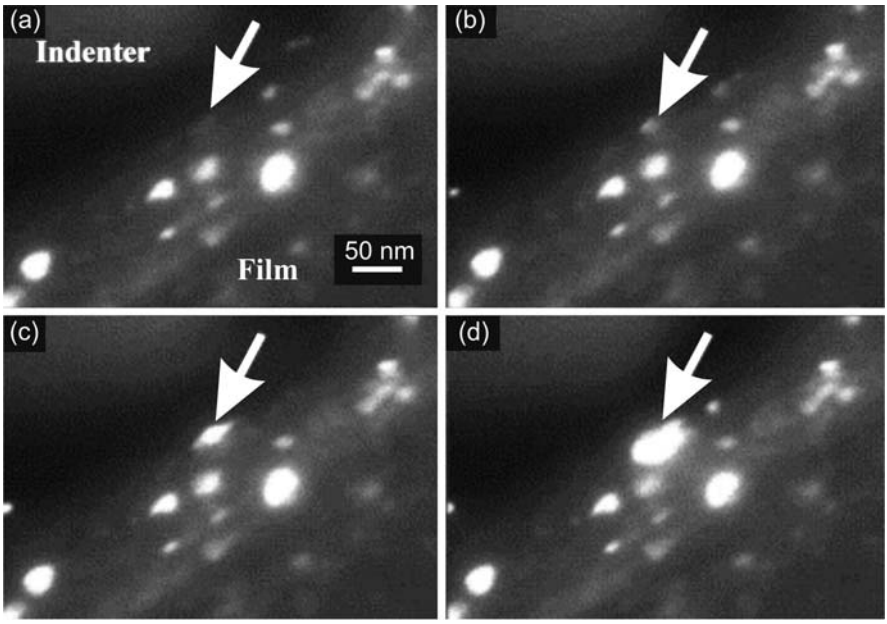

Figure 6-2. Snapshots during in situ TEM nanoindentation of a polycrystalline Al film showing abnormal growth of nano-sized grains. (**a**) No grains in strong diffraction condition under the tip area indicated by the white arrow. (**b**) A grain with size about 10 nm has appeared. (**c**)–(**d**) The size of the grain has become larger with increasing load. Reprinted from [29] with permission from Elsevier

Section 6.5, using both MD and QC methods, we discuss the mechanisms of stress-driven grain growth in nanocrystalline Al during nanoindentation. An outlook for future research in this rich area is also presented in Section 6.6.

6.2. ATOMISTIC MODELING OF NANOSCALE CONTACT IN NANOCRYSTALLINE FILMS

Earlier attempts made to model the nanoindentation of nanocrystalline materials by classical MD simulations have usually employed a spherical repulsive force to model virtual tips varying from 30 to 98 Å in diameter [36–42]. As such, contact areas were, to a large extent, smaller than the grain size, and the plastic zone produced by these tips was only limited to one or two grains. In contrast, Szulfarska et al. [43] have simulated the nanoindentation of normally-brittle nanocrystalline ceramics with a four to one ratio between tip diameter and grain size, which revealed unusual GB-mediated plastic behavior. Different numerical approaches have also been used to study the problems of contact in single-crystal and nanocrystalline films using concurrent multiscale modeling [44–48]. Using the QC method, we show here that it is critically important to simulate nanoindentation tips with more realistic sizes. Furthermore,

atomistic simulations in FCC metals have been performed using different embedded-atom-method (EAM) potentials, from which predictions of stacking fault energies can lead to strong differences within the same metal [49]. The impact of the interatomic potential on cooperative plastic processes, however, is not fully understood. This chapter focuses on the modeling of nanoscale contact in nanocrystalline metal films using MD simulations with LAMMPS [50] and the QC simulation technique [51]. These two methods and specific numerical tools for the analysis of stresses and the visualization of defects and GBs are briefly recalled in the following.

6.2.1. Simulation Methods

6.2.1.1. Molecular Dynamics

Classical MD simulation is a common technique for the numerical investigation of physical and dynamical properties of matter at the molecular level. Each atom in the simulation is treated as a point mass whose velocity and position are computed by time integration of the Newton's equations. The computational task in a typical MD simulation is to solve the set of coupled differential equations given by

$$m_i \frac{d\vec{v}_i}{dt} = \sum_j F_2\left(\vec{r}_i,\vec{r}_j\right) + \sum_j \sum_k F_3\left(\vec{r}_i,\vec{r}_j,\vec{r}_k\right) + \ldots \tag{6-1}$$

$$\frac{d\vec{r}_i}{dt} = \vec{v}_i, \tag{6-2}$$

where m_i is the mass of atom i, $\vec{r}_i$ and $\vec{v}_i$ are its position and velocity vectors, respectively, F_2 is a force function describing pairwise interactions between atoms, F_3 describes three-body interactions, and many-body interactions can be added in the same way. Numerical integration of the atomic positions is usually performed using the Verlet method [52] with a time step, which may be varied from 1 to 5 fs for studies in crystal plasticity. The calculations are also conducted at constant temperature (NVT) using a Nose/Hoover temperature thermostat [53]. Furthermore, the calculations on large-scale systems must take full advantage of massively-parallel computing with open-source MD simulation software such as LAMMPS [50].

6.2.1.2. Quasicontinuum (QC) Method

The QC method, which was developed by Miller and Tadmor [51], is a multiscale atomistic/continuum simulation technique combining both finite element and molecular statics methods. This technique therefore alleviates the need for representing all the atoms as in classical MD simulation. A complete description of the QC method can be found in the review by Miller and Tadmor [51]. A typical QC model consists of atomistic zones (non local) and finite element zones (local). The regions subjected to high plastic deformations are modeled atomically, while the rest is modeled by finite elements. Each node in the mesh is a representative atom, or "repatom", which can either represent just itself (non local zone as well as some

atoms of the atomistic/continuum interface), or a group of atoms (local zone). The total energy of the system is therefore computed such as

$$E_{\text{tot}} = \sum_{\alpha=1}^{N_{\text{rep}}} n_\alpha E_\alpha \approx E_{\text{exact}}, \tag{6-3}$$

where N_{rep} is the total number of repatoms in the system, n_α is the number of real atoms the repatom is representing ($n_\alpha = 1$ for non local atoms), and E_α is the energy of each repatom. This formulation permits to conduct concurrent calculations on both local and non-local regions, which largely decreases the number of degrees of freedom as opposed to MD simulations with corresponding model dimensions. Some discontinuities in energy may also appear at the local/non-local interface, but these can be eliminated by taking ghost forces [51] into account. The minimum energy is calculated at each loading step, after a new set of forces or displacements is applied, using a conjugate gradient method. The QC method can also apply a "nonlocality criterion" to the model in order to verify whether atoms should be local or non-local. This criterion is defined by:

$$\max_{a,b;k} \left| \lambda_k^a - \lambda_k^b \right| < \varepsilon, \tag{6-4}$$

where λ_k^a is the kth eigenvalue of the right stretch tensor $U_a = \sqrt{F_a^T F_a}$ obtained from the deformation gradient F_a in element a, $k = 1\ldots3$, and the indices a and b run over all elements within a cutoff distance of a given repatom. The threshold ε is usually determined empirically, but a value of 10% gives reasonable results in crystal plasticity. If the inequality is not satisfied, the repatom is made non local and vice-versa. It is worth noting that, because of the energy minimization procedure, the QC method can only predict the athermal behavior of crystalline materials at 0 K. Furthermore, Eq. (6-4) may be used with remeshing techniques in order to adapt the finite element mesh as a function of the deformation. Some examples of adaptive QC simulations can be found elsewhere [54, 55].

6.2.2. Modeling of Spherical/Cylindrical Contact in Nanocrystalline Metals

Two methods have been used to model tips in contact problems using atomistic simulation. The first method consists in assuming the tip to be either spherical or cylindrical with a virtual repulsive force such that:

$$F(r) = -k(r - R)^2 \tag{6-5}$$

with k a specified force constant ($k = 10$ N/m^2), R the tip radius, and r the distance between the atom and the center of the tip. This method removes the effects of adhesion and friction that are typically applied by real indenters. Second, the tip can

be modeled by representing all the atoms. If kept rigid, solid tips can be used for direct comparison with different contact theories including adhesion effects [56].

A Voronoi tessellation based on a constrained-Delaunay connectivity scheme [57] is commonly used to model polycrystalline films with randomly-oriented microstructures, i.e. similar to natural GB networks. Reference points are first randomly placed at a specified mean distance from each other in the surface or volume studied. Each reference point becomes the center of a grain whose crystallographic orientation is also randomly assigned. The Voronoi tessellation created from these points forms the network of GBs that are orthogonal to the lines joining the reference point to neighbor reference points as illustrated in Figure 6-3.

In Figure 6-4, we present the use of this methodology to model the indentation of a three-dimensional polycrystalline thin film with a mean grain size of 7 nm. The total number of atoms for such a model is ∼3 million. The film thickness is 30 nm. The film is indented by displacing a spherical tip with a diameter of 18 nm along the direction normal to the top surface. The bottom of the film is fixed along the direction of indentation, while the sides of the model are assigned periodic boundary conditions. The model is first relaxed under zero force condition using a conjugate gradient method in order to obtain the lowest state of energy in the GB network to simulate equilibrium conditions. After relaxation, the tip is moved at a speed on the order of 1 m**.** s^{-1}. The simulation is performed at 300 K with a time step of 5 fs and the atomic positions are recorded at 50 ps intervals (10,000 steps).

Similarly, a QC model of indentation in a 200-nm-thick Al film with a wedge-like cylindrical tip is shown Figure 6-5. In this model, the contact region at the interface between the indenter and the film surface is fully represented by individual atoms. For comparison, the dimensions of both film and fully-atomistic zone are $400 \times 200 \times 0.286$ nm and $50 \times 25 \times 0.286$ nm, respectively. Plane-strain contact is modeled by displacing a single-crystal Al cylinder with a diameter of 30 nm along the direction normal to the film. The tip is oriented along the crystallographic

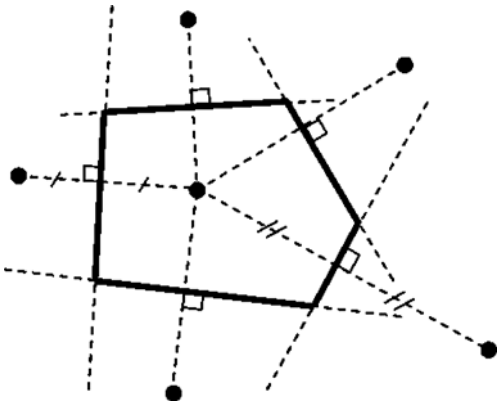

Figure 6-3. Schematic showing the Voronoi construction for a two-dimensional polycrystalline model

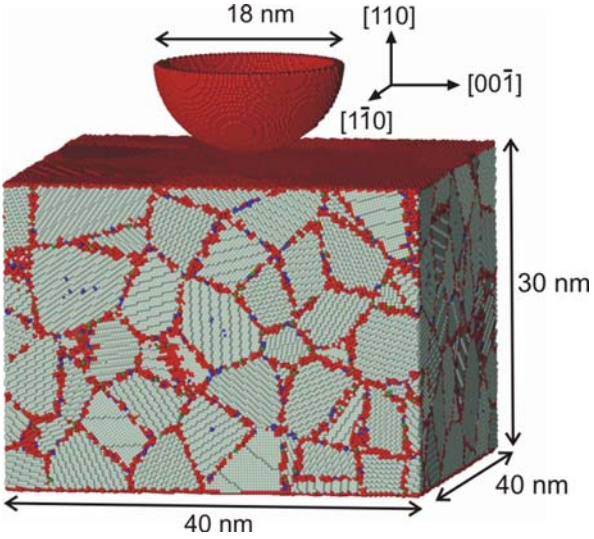

Figure 6-4. Molecular dynamics model of a nanocrystalline thin film to be indented by a rigid, spherical tip. Tip diameter and mean grain size are 18 and 7 nm, respectively. The crystallographic orientations of the tip are as indicated. Periodic boundary conditions are assigned on each side. This model consists of ~3 million atoms

directions shown in Figure 6-5b and kept completely rigid during the simulation. This model consists of ~40,000 atoms.

To avoid discontinuities in the energy state during force minimization, the continuum/atomistic frontier is modeled as a single crystal interface with the crystallographic orientations shown in Figure 6-5a. We note that if the deformation is small (tip penetration < 10 nm), no significant atomistic activity is found near this interface, indicating that the plastic deformation is limited to the polycrystalline region during the simulations. The bottom of the film is fixed along each direction, while both sides of the model are left free. Periodic boundary conditions are imposed along the out-of-plane direction in the entire model. Each grain is assigned a common tilt axis along the [110] direction, and random in-plane orientation. Therefore, this QC model simulates the mechanical behavior of a randomly oriented two-dimensional columnar microstructure, which may differ from that of fully three-dimensional polycrystalline microstructures. Similar to the MD model, the sample is first relaxed under zero pressure condition in order to obtain the equilibrium microstructure. After relaxation, energy minimization by conjugate gradient method is performed between each loading step.

6.2.3. Calculations of Local Stresses and Mean Contact Pressures

In the fully-atomistic zone of QC models, the local stress tensor of the *i*th atom, σ_i, is calculated using the formula provided by Lilleodden et al. [38], which can be simplified as follows:

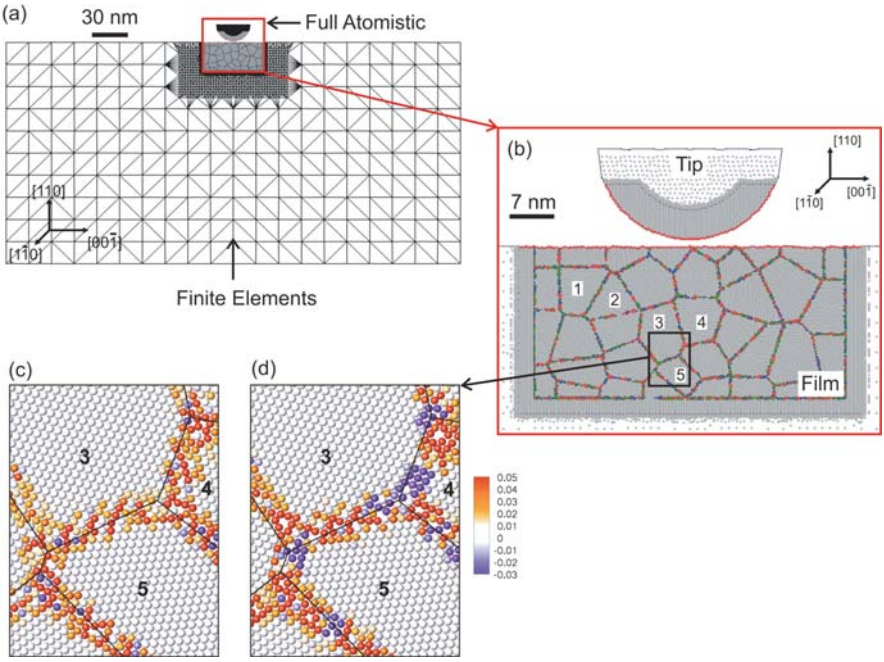

Figure 6-5. Quasicontinuum model of a 7 nm-grain-size Al film indented by a 30-nm-diameter cylindrical tip. (**a**) Full view of both finite element and fully-atomistic regions. (**b**) Close-up view of the full atomistic zone near the contact region. (**c**) Structure and atomic energies at grain boundaries between three nanograins as predicted from the Voter-Chen potential, and (**d**) the Mishin-Farkas potential. Adapted from reference [44] with permission by Elsevier

$$\sigma_i^{\alpha\beta} = \frac{1}{\omega_i^0 \mathrm{Det}[F_i^{\alpha\beta}]} \left\{ \frac{1}{2} \sum_j \left(-\frac{1}{r} \frac{\partial \varphi}{\partial r} \right) r^\alpha r^\beta \Big|_{r=r_{ij}} \right\}, \tag{6-6}$$

where α and β are the Cartesian coordinates, ω_i^0 is the undeformed atomic volume of atom i, $\mathrm{Det}[F_i{}^{\alpha\beta}]$ is the determinant of the deformation gradient, ϕ is the interatomic potential, and r_{ij} is the distance between ith and jth atoms. Note that the kinetics terms have been eliminated in Eq. (6-6) as compared to the formula in [38]. In this equation, the use of the determinant of the deformation gradient has been shown to provide improved accuracy for the calculation of deformed atomic volumes. Furthermore, the force applied by solid tips is calculated using

$$F = \sum_{i \in Z} F_i, \tag{6-7}$$

where Z represents all atoms of the contact area belonging to the film and F_i is the out-of-balance force on atom i in this area, projected along the direction of indentation. The contact area is computed after each loading step by only including atoms at the indenter-film interface within a separation distance from the tip equal to the potential cutoff radius. For wedge-like, cylindrical tips, the mean contact pressure H can be determined at each step such as

$$H = \frac{F}{2a \times z_{\text{perio}}}, \tag{6-8}$$

where a is the contact length, defined as half the width of the projected contact area, and z_{perio} is the sample thickness in the out-of-plane direction.

For virtual tips with a repulsive force, if an atom has penetrated the boundary of the indenter (e.g., $R > r$) after the loading step is completed, the atom is considered "contacted" and feels a force given by Eq. (6-5). The force applied to all contacted atoms is resolved in the direction of indentation, summed and recorded, and is used in the generation of load–displacement profiles [38]. The mean contact pressure is calculated by taking the total applied force on the tip, and by dividing this value by the projected contact area calculated from the position of the contacted atoms.

6.2.4. Tools for the Visualization of Defects and Grain Boundaries

6.2.4.1. Centro-Symmetry Parameter

In solid-state systems, the centro-symmetry parameter P is a useful measure of the local lattice disorder around an atom and can be used to characterize whether the atom is part of a perfect lattice, a local defect (e.g., a dislocation or stacking fault) or at a surface. P is computed using the following formula [58]:

$$P = \sum_{i=1,6} \left| \vec{R}_i + \vec{R}_{i+6} \right|^2, \tag{6-9}$$

where the 12 nearest neighbors are found and R_i and R_{i+6} are the vectors from the central atom to the opposite pair of nearest neighbors. An atom in perfect FCC lattice has a centro-symmetry parameter of zero. The values for other configurations depend on the material chosen. For aluminum, those values are 32.8 Å^2 for a surface atom, 8.2 Å^2 for atoms in an intrinsic stacking fault, and 2.05 Å^2 for atoms halfway between fcc and hcp sites (in a partial dislocation). Equation (6-9) is generally projected in the plane for use with the QC method. In two-dimension, these values are 16.4 Å^2, 4.1 Å^2 and 1.025 Å^2, respectively, for the QC method. The centro-symmetry parameter is well adapted for atomistic simulations at low temperatures, since no averaging for P is needed in these conditions. In the following, atoms in a perfect FCC lattice are either colored in grey or omitted for clarity, those

with a HCP structure or representing a stacking fault are in blue color, and all other non-coordinated atoms appear in green or red colors.

6.2.4.2. Local Crystal Structure by Ackland and Jones

In contrast to the centro-symmetry parameter, the method using the formulation by Ackland and Jones [59] averages out statistical fluctuations due to the temperature boost, because it is not based on the distance between atoms, but the angles between atom pairs. This parameter classifies atoms depending on the closest crystallographic structure it belongs to (BCC, FCC, HCP or unknown). The procedure [59] first calculates the mean squared separation

$$r_0^2 = \sum_{j=1,6} r_{ij}^2 \Big/ 6, \tag{6-10}$$

for the nearest six particles to atom i (i.e., the closest neighbors that verify $r_{ij}^2 < 1.55 r_0^2$). For each of the neighbor pairs found, the bond angle cosines $\cos(\theta_{jik})$ is determined. The procedure, which enables determining the local crystal structure to which atom i can be assigned, relies on a table provided by Ackland and Jones that separates the possible cosine values into 8 ranges. The color scheme used for this parameter is the same than that for the centro-symmetry parameter.

6.3. EFFECTS OF INTERATOMIC POTENTIALS ON EQUILIBRIUM MICROSTRUCTURES

Interactions amongst atoms for FCC metals are represented using an embedded-atom-method (EAM) potential [60], which most accurately predicts the energies of defects and surfaces in such metals. The total energy of a monoatomic system by EAM is described by [61]:

$$E_{\text{tot}} = \frac{1}{2} \sum_{ij} V\left(r_{ij}\right) + \sum_{i} F\left(\bar{\rho}_i\right) \tag{6-11}$$

where $V(r_{ij})$ is a pair potential as a function of the distance r_{ij} between atoms i and j, and F is the embedding energy as a function of the host density $\bar{\rho}_i$ induced at site i by all other atoms in the system. The latter is given by:

$$\bar{\rho}_i = \sum_{j \neq i} \rho(r_{ij}), \tag{6-12}$$

$\rho(r_{ij})$ being the atomic density function. The second term in Eq. (6-11) is volume dependent and represents, in an approximate manner, many-body interactions in the system. EAM potentials are fitted to experimental and ab-initio data for the values

of equilibrium lattice parameter, the cohesive energy, the elastic constants and the vacancy formation energy. This basic set of properties can often be complemented by other data such as planar fault energy and phonon frequencies.

Hereafter, we focus our attention on the effect of EAM interatomic potentials in predicting generalized stacking and planar fault energies, as well as GB energies in equilibrium microstructures. To this end, we compare both the Mishin-Farkas [61] and Voter-Chen [62] potentials for Al. For brevity in the following, these two potentials are referred to as Al-VC and Al-MF potentials, respectively. For each potential, past QC procedures [63, 64] were used to calculate the generalized planar and stacking fault energy curves and the GB energy of 18 Σ <110> tilt bicrystals consisting of symmetrical tilt GBs. The generalized stacking and planar fault energy curves for both potentials are shown in Figure 6-6a. The unstable stacking fault energy (γ_{USF}), stacking fault energy (γ_{SF}) and unstable twinning fault energy (γ_{UTF}) are also indicated in this figure. We find that the calculated energy values are significantly smaller for the Al-VC potential than the Al-MF potential, which is consistent with the predicted values in the literature [61]. In addition, we find that all the ratios γ_{SF}/γ_{USF} and $\gamma_{UTF}/\gamma_{USF}$ are similar and equal to 0.81–0.86 and 1.30–1.32, respectively, which suggests the same slip and twinning behavior regardless of the interatomic potential for Al [65]. Figure 6-6b also shows a significant increase in GB energy for the symmetric tilt bicrystals from the Al-VC potential to the Al-MF potential. The difference of GB energy at atomic level, as a function of EAM potential, is also clearly shown in Figures 6-5c and d, where a cluster of three nanograins is represented. Both atomic energies and structures at GBs are dramatically changed by the interatomic potential, despite the same misorientation angles between grains. This observation therefore indicates that the bonding properties of the GBs will be markedly different depending on the potential.

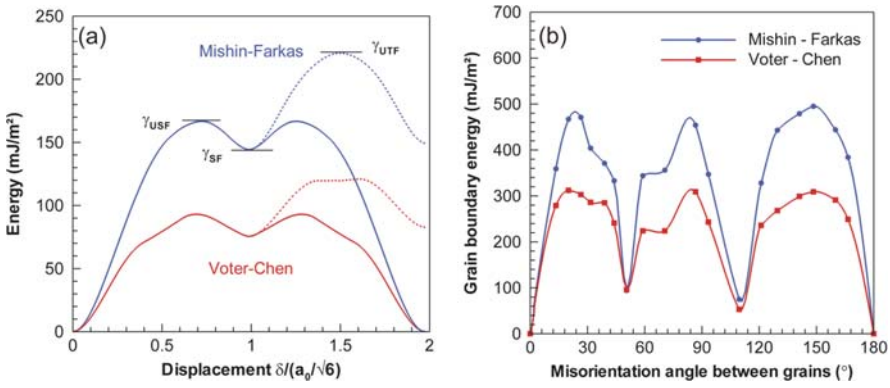

Figure 6-6. Comparison of the Mishin-Farkas and Voter-Chen EAM potentials for Al by QC method for (**a**) the generalized stacking fault energy (*solid line*) and planar fault energy (*dashed line*) curves, and (**b**) GB energies in symmetrical <110>-tilt bicrystals

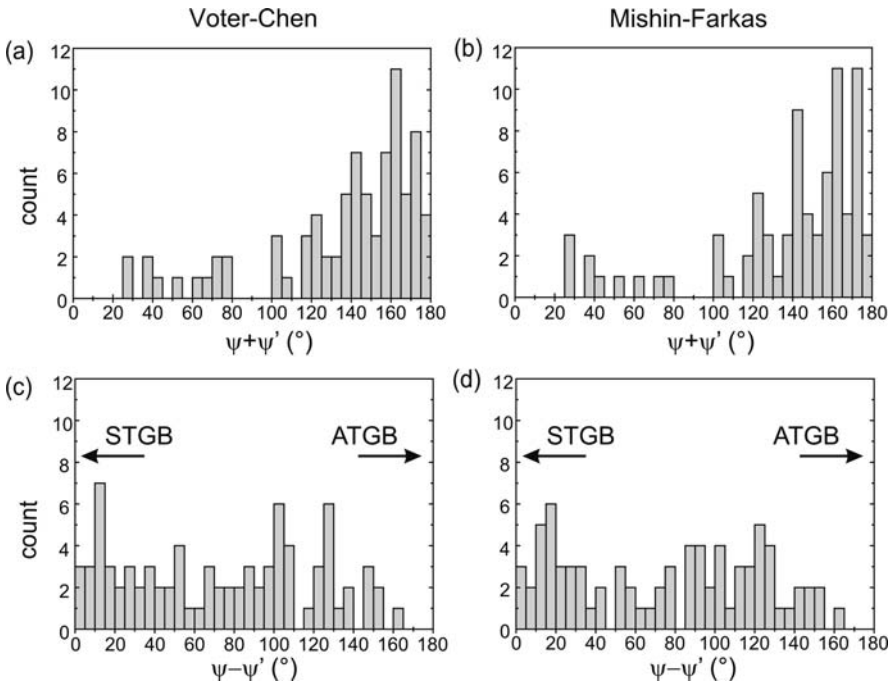

Figure 6-7. Effects of EAM potentials on equilibrium microstructures in the simulated nanocrystalline Al film shown in Figure 6-5. (**a**)–(**b**) Distribution of misorientation angles ($\psi + \psi'$) between grains. (**c**)–(**d**) Degree of symmetry of the GB structure from perfectly-symmetrical tilt GB (STGB, $\psi - \psi' \sim 0$) to highly-asymmetrical tilt GB (ATGB, $\psi - \psi' \sim 180°$). Reprinted from [44] with permission from Elsevier

Furthermore, the effect of potential is investigated on the misorientation angle and asymmetry of the GBs in the 7-nm-grain-size microstructure shown in Figure 6-5. Figure 6-7 shows the angles ψ and ψ', which represent the angle between the [110] lattice direction and the GB plane for two neighboring grains, respectively. The sum $\psi + \psi'$ characterizes the misorientation angle at the boundary separating two grains. Some minor differences in the misorientation angle $\psi + \psi'$ are observed due to the rearrangement of microstructure after relaxation, even though the original model is identical. It can however be concluded from Figures 6-7a and b that the distribution of misorientation angle and, therefore, the overall microstructure of the GB network are not significantly affected by the potential. In addition, the difference $\psi - \psi'$ represents the degree of symmetry of the GB, where $\psi - \psi' = 0°$ corresponds to perfectly-symmetric tilt GBs, and $\psi - \psi' = 180°$ to highly-asymmetric tilt GBs. In Figures 6-7c and d, the degree of symmetry is found to be homogeneous along the set of values for $\psi - \psi'$ regardless of the potential.

In summary, the two EAM potentials for Al mostly differ in their prediction of the generalized stacking and planar fault energies, and GB energies, but should not significantly influence the grain morphology at equilibrium and slip behavior in the material.

6.4. EFFECTS OF A GRAIN BOUNDARY NETWORK ON INCIPIENT PLASTICITY DURING NANOSCALE CONTACT

Shear banding is an important mode of plastic deformation in nanocrystalline materials, and is best illustrated by a 5 nm-grain-size simulation using the Al-VC potential (Figure 6-8). At the onset of plasticity, significant GB sliding takes place leading to rotational deformation of the grains with limited intragranular slip. During this process, the GB structure is significantly changed and, in some cases, several GBs tend to be aligned (Figure 6-8b). The bands are formed by the sliding of aligned interfaces separating the grains (see for example grains 3 and 4 in Figure 6-8c). When the shear plane encounters a triple junction and is stopped by a grain that is not in its alignment, the shear band follows its path by intragranular slip in the prolongation of the shear plane. For example, a stacking fault left behind a partial dislocation can be seen in grain 2 in the prolongation of the shear plane in Figure 6-8b. Subsequently, the newly created stacking faults are found to nucleate mechanical twins, which grow under the applied shear stress. Mechanical twinning has also been observed in nanocrystalline Al under indentation by Chen et al. [28] (This result therefore suggests that there is good agreement between simulation and experimental data).

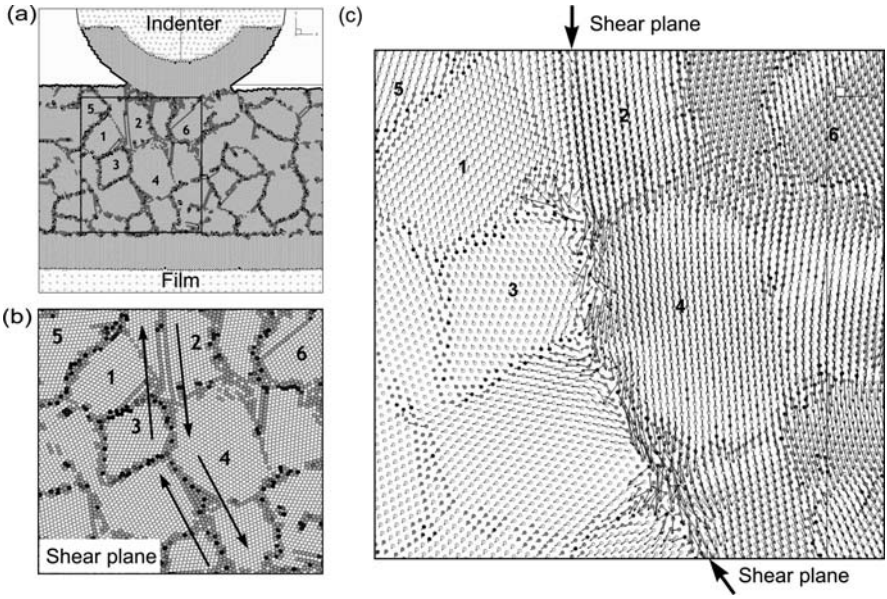

Figure 6-8. Formation of a thin shear band in a 5-nm-grain-size nanocrystalline Al during indentation by QC method. (**a**) Partial view of the contact interface and location of the grain cluster associated with the shear band. (**b**) Close up view of the shear plane. (**c**) Magnitude and direction of atomic displacements between two loading increments shown by arrows. Reprinted from [47] with permission from Elsevier

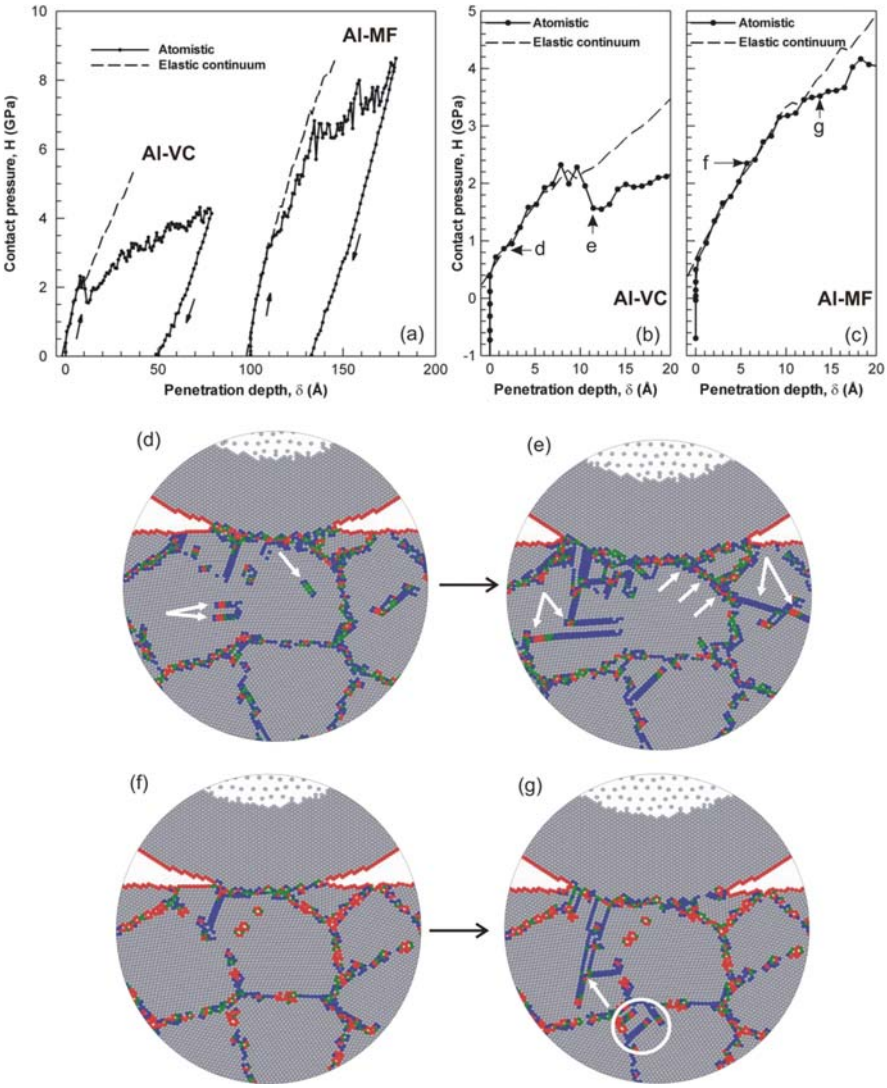

Figure 6-9. Effects of EAM potential on the mean contact pressure as a function of penetration depth in a 7 nm-grain-size QC simulation. (**a**)–(**c**) Loading and unloading responses with Voter-Chen (Al-VC) and Mishin-Farkas (Al-MF) EAM potentials for Al. Snapshots showing the deformation in the film near the contact region for different stages of indentation for (**d**)–(**e**) the Al-VC potential, and (**f**)–(**g**) the Al-MF potential. Adapted from [44] with permission from Elsevier

Furthermore, Figure 6-9 represents the evolution of the mean contact pressure as a function of penetration depth for both the Al-VC and Al-MF potentials. A fitting between atomistic simulation and elastic continuum theory [44] shows an excellent agreement in the initial portion of the curves. Both curves also show clear

evidence of flow serration at large depths of indentation, which is consistent with the formation of shear bands. In Figure 6-9, however, the plastic flow serration is somewhat less intense with the Al-VC potential than the Al-MF potential. In the latter, a clear change in slope occurs for a penetration depth of 34 Å, which corresponds to the propagation of an extensive shear band by intragranular slip through several grains (not shown). Furthermore, Figures 6-9b and c reveal that the contact pressures are almost identical between atomistic results and elastic theory until the two curves reach a depth of 10–15 Å. The divergence between elastic and atomistic curves marks the onset of plasticity from a macroscopic, continuum standpoint. These curves also provide direct evidence that the onset of plasticity occurs at significantly larger contact pressure in the Al-MF potential than the Al-VC potential. The pressure difference becomes even more significant at the end of the indentation process, where contact pressures of 4.3 and 8.6 GPa are observed for the two potentials, respectively. Investigation of the depth of the residual impression after unloading also shows some significant differences in the constitutive response between the two potentials.

The change in nanoindentation behavior can be largely interpreted from fundamental differences in plastic deformation mechanisms at GBs as a function of potential. While the nucleation of a few dislocations takes place at the tip/substrate contact interface during the elastic portion of the contact curves with both potentials (Figures 6-9d and f), more GB-mediated activity in the substrate occurs with the Al-VC potential. Here, GB-mediated plasticity is characterized by one of the following mechanisms: (1) the emission of partial dislocations and twins emanating from GBs, along with their propagation through intragranular slip, (2) GB sliding and grain rotation, and (3) stress-driven GB migration coupled to shear deformation.

6.5. MECHANISMS OF GRAIN BOUNDARY MOTION DURING CONTACT PLASTICITY

Several mechanisms for grain growth have been investigated in nanocrystalline metals. These can primarily be divided into two categories: Thermally-driven mechanisms and stress-assisted mechanisms (Figure 6-10). The first category is related to curvature-driven GB motion [66] (Figure 6-10a). During this process, the GB tends to move towards the center of the curvature to reduce the total area of GBs, and thus the energy of the system [67]. Another thermally-driven mechanism is GB atom diffusion [68], during which the atoms jump in the crystal into point vacancies, creating a new vacancy in the process.

The last two mechanisms in Figure 6-10 represent stress-assisted mechanisms, which can make grain growth at cryogenic temperatures possible [31]. The first mechanism corresponds to rotation-induced grain coalescence [67], during which one grain rotates in order to match the orientation of a neighbor grain, thus forming a single larger grain (Figure 6-10d). This process is often associated with GB sliding [69]. The second mechanism of strain-driven grain growth is related to shear-coupled GB motion (Figure 6-10e). In this case, the normal motion of

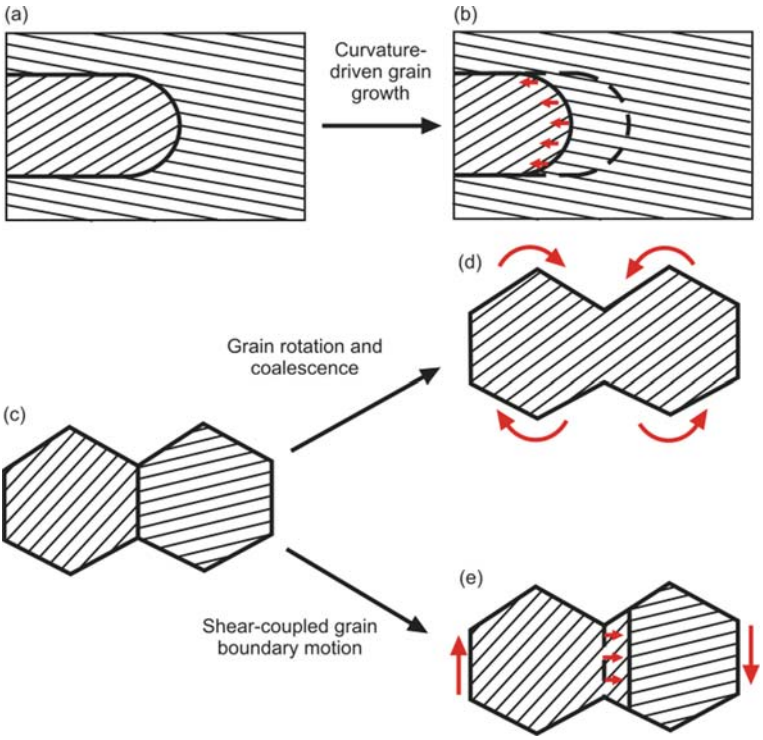

Figure 6-10. Schematic illustrations of different mechanisms of GB motion in metals. (**a**)–(**b**) Thermally-driven GB motion. (**c**) Strain-driven GB motion by either (**d**) grain rotation and coalescence or (**e**) shear-coupled GB migration

GBs results from a shear strain applied tangentially to them and causing tangential motion, or coupled motion [69–72].

To illustrate such grain growth mechanisms during indentation, Figure 6-11 presents the indentation of a 7-nm-grain-size Al film by a spherical tip from MD simulation at 300 K. In this figure, the GB atoms and lattice defects appear in white color, and the other atoms are colored according to the grain they belonged to at the beginning of the simulation. Several major grain growth events are visible in Figure 6-11: between grains 1 and 2, between grains 3 and 4, for grains 5, 6, 7 and 8, which all appear to be strain-driven as demonstrated below.

The grain growth events occurring between grains 1 and 2 and between grains 3 and 4, starts very early in the indentation process. A closer inspection of the evolution of these grains shows that the misorientation angles at the GB are very small before relaxation, which makes them low-angle GBs. After relaxation, the grains slightly rotate, until the misorientation angle is low enough to have the atoms at the interface in perfect FCC arrangement. The corresponding mechanism of GB migration is therefore rotation-induced grain coalescence.

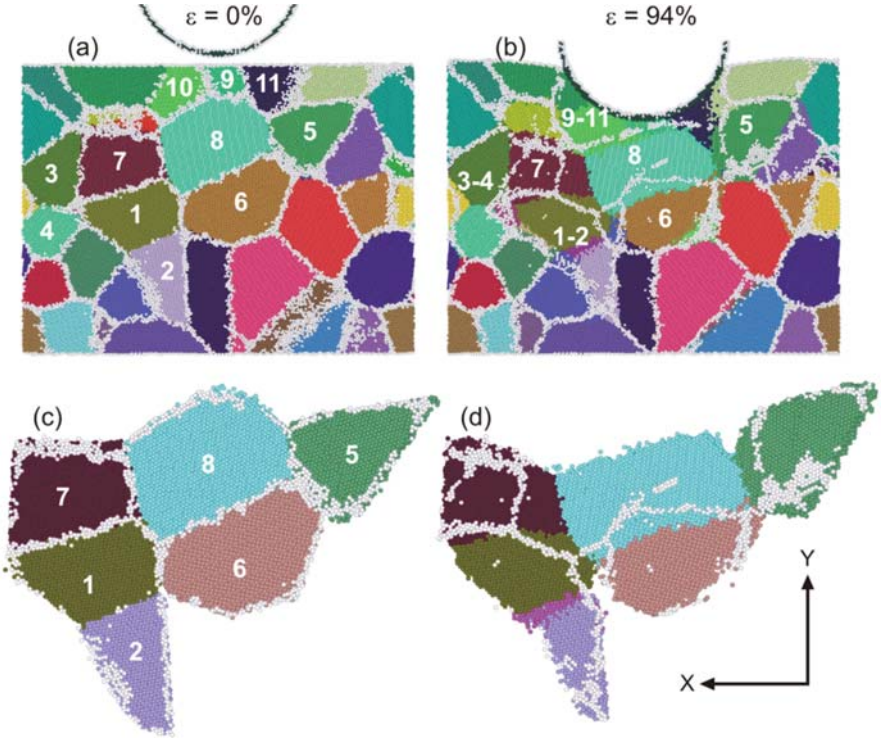

Figure 6-11. Three-dimensional MD simulation of microstructure evolution in nanocrystalline Al indented by a 9 nm-radius Al tip. General view obtained (**a**) after relaxation and before indentation ($\varepsilon = 0\%$) and (**b**) at maximum indentation ($\varepsilon = 94\%$). (**c**) Close-up view of grains 1, 2, 5, 6, 7 and 8 when (**c**) $\varepsilon = 0\%$ and (**d**) $\varepsilon = 94\%$ [48]

The deformation process in grains 5, 6, 7 and 8 is clearly different from that in grains 1, 2, 3 and 4, because the boundaries are followed moving across neighbor grains (Figure 6-11d). We find that the rate of GB migration can be strongly decreased as the tip radius decreases which tends to indicate that this mechanism depends on the local strain. Furthermore, the shape of grain 7 evolves from originally square to trapezoidal after migration of the interface between grains 7 and 8. These results suggest that the process of GB migration is coupled to shear deformation in this case. In this process, grains 6 and 8 have grown, while grains 5 and 7 have notably decreased in diameter. Also a new grain was grown at the triple junction of grains 1, 6 and 8.

However, MD simulation makes the analysis of strain-driven GB motion difficult due to the implications of thermal effects. In contrast, QC simulations, which operate at zero temperature, may readily eliminate those effects. For example, Figure 6-12 shows the motion of the interface separating grains 3 and 5, which corresponds to a high-angle GB ($\psi + \psi' = 160.7°$), from the QC simulation presented in Figure 6-5 with the use of the Al-VC potential.

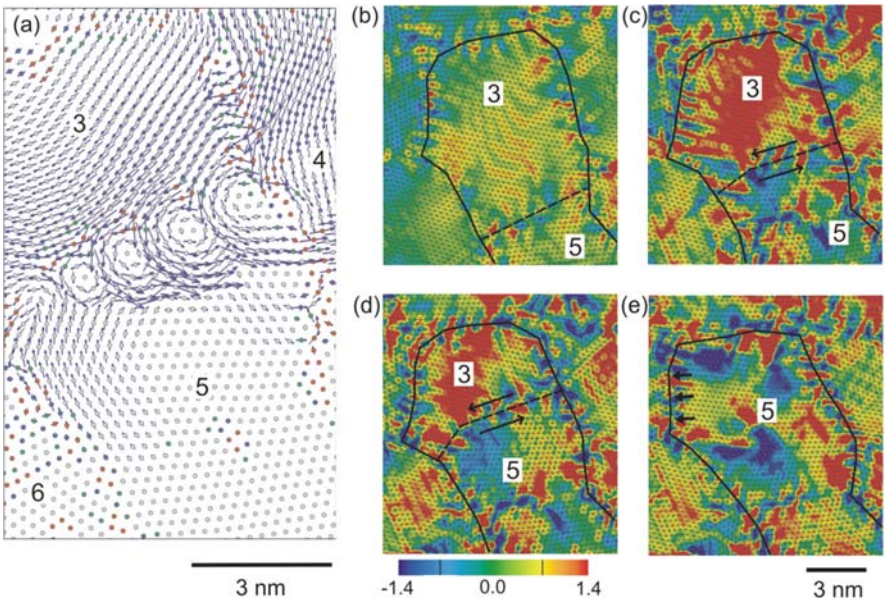

Figure 6-12. QC simulation of shear-coupled GB motion in nanocrystalline Al during indentation. (**a**) Local lattice rotations at GB forming vortex-like patterns. (**b**)–(**e**) Snapshots showing the evolution of the atomic-level shear stress relative to the orientation of the interface between grains (in units of GPa). The boundaries of grains 1 and 2 have been highlighted for clarity. Adapted with permission from [46].

Each stress map represented in Figure 6-12 corresponds to a different loading level taken from before the start of the migration to the end of the GB motion. It is found that the interface migration process causes a strong stress relief in the GB network. Furthermore, the sign of the stress, indicated by the color blue or red in Figure 6-12 indicates that the GB between grains 3 and 5 is under shear stress, one side being under positive stress, and the other under negative stress. In this GB migration process, it is clear that the size of grain 5 has increased at the expense of grain 3. Therefore, this analysis shows clear evidence that the mechanism of stress-assisted grain growth corresponds to shear-coupled motion.

Furthermore, Figure 6-13 shows that GB migration is only observed for the Al-VC simulation. The original position of the GB before indentation is indicated by a dashed line for reference. The GB in the Al-VC simulation has moved about 34 Å into grain 3, whereas no significant differences are found with the Al-MF simulation, other than some minor rearrangements of GB atoms.

In summary, the mechanism of stress-driven grain growth was found associated with shear-coupled GB motion, rather than by rotation-induced grain coalescence. We can therefore conclude that the plastic flow is found enhanced in the case of the Al-VC simulation because of the increased GB deformation activity in the form of GB sliding and coupled GB motion at both 0 and 300 K. This finding could therefore

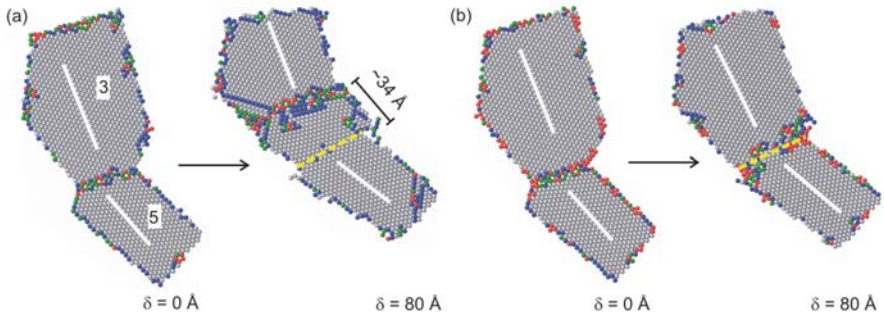

Figure 6-13. Effects of EAM potential on the shear-coupled GB migration between grains 3 and 5 as shown in Figure 6-6, as a function of penetration depth δ. (**a**) Voter-Chen potential. (**b**) Mishin-Farkas potential. Reprinted from [44] with permission from Elsevier

suggest a new means to control stress-assisted grain growth mechanisms by altering the local structure and energies at GBs.

6.6. CONCLUDING REMARKS

In this chapter, we describe two computational approaches using either MD or QC methods to investigate the complexity of plastic deformation and yielding in nanocrystalline GB networks under nanoscale contact. These approaches show that the interatomic potentials play a key role in the prediction of equilibrium structures and energies at GBs, which in turn has a strong influence on the mechanisms of plasticity mediated by GBs, such as GB-mediated crystal slip, GB sliding, grain rotation and GB migration. It is also demonstrated that shear-coupled GB motion due to the strain applied by penetrating tips, is an important mechanism of grain growth and plasticity at both absolute zero and room temperature.

An outlook for future research in this area can be summarized by asking two fundamental questions. First, can the addition of impurities significantly influence the simulation of GB-mediated plasticity in nanocrystalline metals? It is acknowledged that solute impurities, like H and O impurities in Al, have strong impact on stacking fault and GB energies, and plasticity in FCC metals [32, 73–75]. To this end, proper numerical formalisms, such as local chemical potential [75], should be developed to include impurities in multiscale simulations. Second, how do the geometry and deformation of tips influence plasticity induced by nanoscale contact in nanocrystalline materials? Clearly, present simulations do not take into account the finite-temperature deformation of the tips. Atomistic simulation on this aspect may provide more fundamental understanding of tip-film interactions, which may ultimately help engineers explore new routes for high-throughput nanomanufacturing technology, such as nanoimprint lithography [76].

ACKNOWLEDGMENT

Support from National Science Foundation CAREER program (grant no DMR-0747658) and the computational resources provided by the Vermont Advanced Computing Center, which is supported by NASA (grant no NNX 06AC88G), are gratefully acknowledged.

REFERENCES

1. Basrour, S. and Robert, L. (2000) Mater. Sci. Eng. A 288: 270–274.
2. Gobet, J., Cardot, F., Bergqvist, J. and Rudolf, F. (1993) J. Micromech. Microeng. 3: 123–130.
3. Larsen, K.P., *et al*. (2003) Sens. Actuators A 103: 156–164.
4. Martinez, S., *et al*. (2002) Sens. Actuators A 99: 41–44.
5. Pasa, A.A. and Schwarzacher, W. (1999) Phys. Stat. Sol. A 173: 73.
6. Krauss, A.R., *et al*. (2001) Diam. Relat. Mater. 10: 1952–1961.
7. Tao, S. and Li, D.Y. (2006) Nanotechnology 17: 65–78.
8. Schiotz, J. and Jacobsen, K.W. (2003) Science 301: 1357–1359.
9. Trelewicz, J.R. and Schuh, C.A. (2007) Acta Materialia 55: 5948–5958.
10. Chang, S.Y. and Chang, T.K. (2007) J. Appl. Phys. 101: 033507.
11. Tsuchiya, T., Tabata, O., Sakata, J. and Taga, Y. (1996) IEEJ Trans. 116: 441.
12. Sharpe, W.N., Yuan, B. and Edwards, R.L. (1997) J. Microelectromech. Syst. 6: 193–199.
13. Chasiotis, I. and Knauss, W.G. (2002) Exp. Mech. 42: 51–57.
14. Hemker, K.J. and Sharpe, W.N. (2007) Annu. Rev. Mater. Res. 37: 93–126.
15. Espinosa, H.D., Prorok, B.C. and Fischer, M. (2003) J. Mech. Phys. Solids 51: 47–67.
16. Nieman, G.W., Weertman, J.R. and Siegel, R.W. (1989) Scripta Metall. 23: 2013–2018.
17. Elsherik, A.M., Erb, U., Palumbo, G. and Aust, K.T. (1992) Scripta Metall. Mater. 27: 1185–1188.
18. Fougere, G.E., Weertman, J.R. and Siegel, R.W. (1995) Nanostruct. Mater. 5: 127–134.
19. Qin, X.Y., Wu, X.J. and Zhang, L.D. (1995) Nanostruct. Mater. 5: 101–110.
20. Farhat, Z.N., Ding, Y., Northwood, D.O. and Alpas, A.T. (1996) Mater. Sci. Eng. A 206: 302–313.
21. Malow, T.R., Koch, C.C., Miraglia, P.Q. and Murty, K.L. (1998) Mater. Sci. Eng. A 252: 36–43.
22. Sanders, P.G., Eastman, J.A. and Weertman, J.R. (1997) Acta Mater. 45: 4019–4025.
23. Gang, T. and Sansoz, F. (2007) Unpublished Research.
24. Minor, A.M., *et al*. (2006) Nat. Mater. 5: 697–702.
25. Yang, B. and Vehoff, H. (2007) Acta Materialia 55: 849–856.
26. Andrievski, R.A., Kalinnikov, G.V., Jauberteau, J. and Bates, J. (2000) J. Mater. Sci. 35: 2799–2806.
27. Van Vliet, K.J., Tsikata, S. and Suresh, S. (2003) Appl. Phys. Lett. 83: 1441–1443.
28. Chen, M.W., *et al*. (2003) Science 300: 1275–1277.
29. Jin, M., Minor, A.M., Stach, E.A. and Morris, J.W. (2004) Acta Materialia 52: 5381–5387.
30. Zhang, K., Weertman, J.R. and Eastman, J.A. (2004) Appl. Phys. Lett. 85: 5197–5199.
31. Zhang, K., Weertman, J.R. and Eastman, J.A. (2005) Appl. Phys. Lett. 87: 061921.
32. Gianola, D.S., *et al*. (2006) Acta Materialia 54: 2253–2263.
33. Hall, E.O. (1951) Proc. Phys. Soc. B 64: 747–753.
34. Petch, N.J. (1953) J. Iron Steel Inst. 174: 25–28.
35. Schiotz, J., Di Tolla, F.D. and Jacobsen, K.W. (1998) Nature 391: 561–563.
36. Feichtinger, D., Derlet, P.M. and Van Swygenhoven, H. (2003) Phys. Rev. B 67: 024113.
37. Ma, X.L. and Yang, W. (2003) Nanotechnology 14: 1208–1215.
38. Lilleodden, E.T., Zimmerman, J.A., Foiles, S.M. and Nix, W.D. (2003) J. Mech. Phys. Solids 51: 901–920.
39. Hasnaoui, A., Derlet, P.M. and Van Swygenhoven, H. (2004) Acta Materialia 52: 2251–2258.

40. Jang, H. and Farkas, D. (2004) Mater. Res. Soc. Symp. Proc. 821: P8.17.1–P8.17.6.
41. Saraev, D. and Miller, R.E. (2005) Model. Simulat. Mater. Sci. Eng. 13: 1089–1099.
42. Kim, K.J., Yoon, J.H., Cho, M.H. and Jang, H. (2006) Mater. Lett. 60: 3367–3372.
43. Szlufarska, I., Nakano, A. and Vashishta, P. (2005) Science 309: 911–914.
44. Dupont, V. and Sansoz, F. (2008) Acta Mater. 56: 6013–6026.
45. Luan, B.Q., *et al*. (2006) Phys. Rev. E 74: 11.
46. Sansoz, F. and Dupont, V. (2006) Appl. Phys. Lett. 89: 111901.
47. Sansoz, F. and Dupont, V. (2007) Mater. Sci. Eng. C 27: 1509–1513.
48. Dupont, V. (2008) Ph.D. Thesis. University of Vermont.
49. Zimmerman, J.A., Gao, H.J. and Abraham, F.F. (2000) Model. Simulat. Mater. Sci. Eng. 8: 103–115.
50. Plimpton, S. (1995) J. Comput. Phys. 117: 1–19.
51. Miller, R.E. and Tadmor, E.B. (2002) J. Comput. Aid Mater. Des. 9: 203–239.
52. Rapaport, D.C. (2004) The Art of Molecular Dynamics Simulation. Cambridge University Press, Cambridge, UK, 549.
53. Hoover, W.G. (1985) Phys. Rev. A 31: 1695–1697.
54. Shenoy, V.B., *et al*. (1999) J. Mech. Phys. Solids 47: 611–642.
55. Sansoz, F. and Molinari, J.F. (2007) Thin Solid Films 515/6: 3158–3163.
56. Johnson, K.L. (1985) Contact Mechanics. Cambridge University Press, Cambridge, UK, 452.
57. Voronoi, G.F. (1908) J. Reine Undangew. Math. 134: 199–287.
58. Kelchner, C.L., Plimpton, S.J. and Hamilton, J.C. (1998) Phys. Rev. B 58: 11085–11088.
59. Ackland, G.J. and Jones, A.P. (2006) Phys. Rev. B 73: 054104.
60. Daw, M.S. and Baskes, M.I. (1983) Phys. Rev. Lett. 50: 1285–1288.
61. Mishin, Y., Farkas, D., Mehl, M.J. and Papaconstantopoulos, D.A. (1999) Phys. Rev. B 59: 3393–3407.
62. Voter, A.F. and Chen, S.P. (1987) Mater. Res. Soc. Symp. Proc. 82: 175.
63. Sansoz, F. and Molinari, J.F. (2005) Acta Materialia 53: 1931–1944.
64. Sansoz, F. and Molinari, J.F. (2004) Scripta Materialia 50: 1283–1288.
65. Van Swygenhoven, H., Derlet, P.M. and Froseth, A.G. (2004) Nat. Mater. 3: 399–403.
66. Zhang, H., Upmanyu, N. and Srolovitz, D.J. (2005) Acta Materialia 53: 79–86.
67. Haslam, A.J., *et al*. (2001) Mater. Sci. Eng. A 318: 293–312.
68. Huntington, H.B. and Seitz, F. (1942) Phys. Rev. 61: 315.
69. Cahn, J.W., Mishin, Y. and Suzuki, A. (2006) Acta Materialia 54: 4953–4975.
70. Cahn, J.W. and Taylor, J.E. (2004) Acta Materialia 52: 4887–4898.
71. Gutkin, M.Y., Mikaelyan, K.N. and Ovid'ko, I.A. (2008) Scripta Materialia 58: 850–853.
72. Gutkin, M.Y. and Ovid'ko, I.A. (2005) Appl. Phys. Lett. 87: 251916.
73. Lu, G., Zhang, Q., Kioussis, N. and Kaxiras, E. (2001) Phys. Rev. Lett. 8709: 095501.
74. Lu, G., *et al*. (2002) Phys. Rev. B 65: 064102.
75. Elsener, A., Politano, O., Derlet, P.M. and Van Swygenhoven, H. (2008) Model. Simulat. Mater. Sci. Eng. 16: 025006.
76. Chou, S.Y., Krauss, P.R. and Renstrom, P.J. (1996) J. Vac. Sci. Technol. B 14: 4129–4133.